AIAA JOURNAL
Vol. 60, No. 5, May 2022

Onset of Oblique Detonation Waves for a Cavity-Based Wedge

Li Yang,* Lianjie Yue,† and Qifan Zhang‡
State Key Laboratory of High Temperature Gas Dynamics, Institute of Mechanics, Chinese Academy of Sciences, 100190 Beijing, People's Republic of China

https://doi.org/10.2514/1.J060922

To shorten the ignition length of the wedge-induced oblique detonation wave, a geometric setup in which the leading and aft wedges are connected by a cavity is proposed. High-resolution viscous computations to solve the reactive Reynolds-averaged Navier–Stokes equations have been performed, which examine the onset and evolution of combustion and flow configuration with premixed mixtures of inflow Mach numbers ranging from 4.0 to 6.0. The unreactive flowfield of the cavity-based wedge is analogous to that of a sole cavity with the exclusion of shock/shock interaction downstream. For $Ma = 4.0$ and 5.0, no sustainable oblique detonation wave is achieved, and the flame holds in the cavity and near-wall area of the aft wedge; however, a short-lived detonation wave triggered by the shock focuses is observed during the combustion procedure with $Ma = 5.0$. For $Ma = 6.0$, nearly direct detonation initiation of postshock occurs, and an oblique detonation wave is established above the fore edge of the cavity. Unexpectedly, a delayed ignition downstream contributes to the development of a recirculation zone, which results in a detached oblique detonation wave for $Ma = 5.5$.

Nomenclature

C_f	=	skin-friction coefficient
D	=	diffusion coefficient
E	=	total energy per mass
E_a	=	activation energy
K	=	pre-exponential factor
k	=	thermal conductivity coefficient
L_{SB}	=	length of separation bubble
l_{ign}	=	induction ignition length
l_{ref}	=	reference length
Ma	=	Mach number
p	=	pressure
Q	=	heat release of chemical reaction
R	=	specific gas constant
T	=	temperature
t_{ind}	=	chemical induction time
u	=	velocity in the x direction
u_{OSW}	=	postshock velocity
v	=	velocity in the y direction
γ	=	specific heat ratio
θ	=	wedge angle
λ	=	chemical reaction progress variable
μ	=	dynamics viscosity coefficient
ρ	=	density
τ	=	viscous shear stress
ω	=	chemical reaction rate

Subscripts

b	=	burned state
eff	=	effective
I	=	induction zone
R	=	exothermic reaction zone
s	=	postshock state
u	=	unburned state
∞	=	quantities of the free inflow stream

Received 20 May 2021; revision received 28 October 2021; accepted for publication 30 October 2021; published online 10 January 2022.

*Ph.D. Candidate; also School of Aerospace Engineering, Beijing Institute of Technology, Beijing 100081, China; yangli991@hotmail.com.

†Professor; also School of Engineering Sciences, University of Chinese Academy of Sciences, Beijing 100049, China; yuelj@imech.ac.cn (Corresponding Author).

‡Assistant Professor; also School of Engineering Sciences, University of Chinese Academy of Sciences, Beijing 100049, China; zhangqifan@imech.ac.cn.

I. Introduction

DETONATION waves are supersonic-traveling reactive waves that are accompanied by energy release and a distinguished increase of thermodynamic parameters in a minute time and space scale across it [1]. Theoretically, Chapman–Jouguet (CJ) detonation has a higher thermodynamic cycle efficiency than constant-pressure combustion [2]. Detonation propulsion has been a promising power device in the air-breathing hypersonic flight field, and certain concepts such as pulsed detonation engines, oblique detonation wave engines (ODWEs), and rotating detonation engines are suggested [3,4], which attract a substantial amount of research and development for practical implementation. One of the ODWE models is depicted in Fig. 1 [5], in which the fuel/oxidizer mixing and the combustion procedure are segregated. In the inlet of the engine (vehicle forebody), the mixing process is arranged, which should avoid or delay the ignition of premixed mixtures. Combustion occurs on the wedge downstream, where reactants are ignited by the oblique shock wave (OSW). In particular, shock-wave coupling with combustion leads to the formation of detonation. In certain reports, ODWEs belong to one kind of shock-induced combustion ramjet (shcramjet) [6], which has comparable performance to the scramjet engine with the exceptional benefits of reduced engine size and increased thrust yielded from pressure-gain combustion. A ground test of the designed standing oblique detonation ramjet with a hypersonic flight-duplicated shock tunnel is conducted, and a standing oblique detonation wave (ODW) is obtained, which lasts 50 ms long at $Ma = 9$ inflow. Experimental verification demonstrates that ODWE can be performed steadily under hypersonic flow conditions [7].

The typical wave configuration depicted in Fig. 1, named delayed ODW in which a triple point unites an inert OSW emanating from the wedge tip, a combustion wave (CW) developed from the wedge surface, and an oblique detonation front [8], is proved via limited experimental investigations and vast amounts of numerical studies. Additional experimental works in which a hypersonic projectile is launched into premixed flammable mixtures determine various ODW categories, such as strong overdriven, weak overdriven, and quasi-CJ detonation wave [9]. The main work on wedge-induced ODW is numerically conducted, inasmuch as it is arduous to experimentally acquire the supersonic, reactive, oncoming flow and trigger an ODW by the wedge.

Considerable numerical simulations to solve the Euler equations focus on the OSW to ODW transition mode of delayed ODW and the cellular-like structure of the ODW front [10]. Various factors are

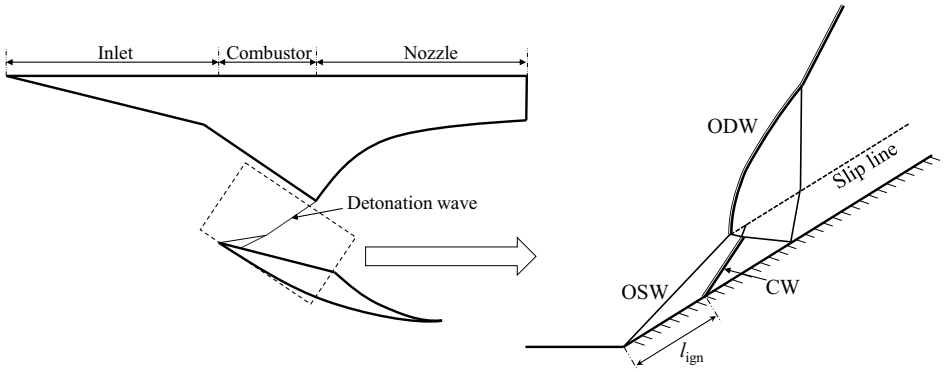

Fig. 1 Schematic depiction of oblique detonation wave engine and its classic flowfield.

proposed to forecast the transition patterns, such as the critical Mach number [11], ratio of the induction time to the total reaction time [12], and ratio of the inflow velocity to CJ detonation velocity [13]. The wave structures near the triple point have also attracted interest [14,15], and λ-shaped, X-shaped and Y-shaped shock configurations with different inflow Mach numbers have been observed and analyzed. The cellular structure and instability of the ODW front were influenced by different factors [16–18], such as the activation energy, wedge angle, and Mach number. The pattern of cellular structure is mainly controlled by transverse waves, for example, left-running transverse waves and right-running transverse waves, which are caused by the variation in the reaction zone thickness due to the spatial or temporal oscillation of the leading shock front. Additionally, the control of ODWs can provide guidelines for the engineering application of ODWEs. The quasi-CJ ODW can be established with proper wave angles in a double-wedge configuration [19], in which the expansion wave plays a role in the formation of the ODW [20]. Furthermore, two wedges connected with a plain step induce a high-temperature and low-velocity zone, which can significantly decrease the induction length of the ODW, and the wedge geometry can control the trigger location with a narrow Mach number range of 6.4–7.0 [21]. The geometric settings, such as the leading wedge angle, step angle, and depth, are considered in the initiation of the oblique detonation wave [22]. The hot jet located on the wedge surface [23] and coflow hot jet at backward step [24] can trigger ODW at the given location and obviously shorten the induction length. The injection pressure and velocity of a hot jet are selected to study the initiation characteristics.

Nevertheless, few viscous detonation simulations have been carried out. The viscous effect on the ignition, evolution, and stabilization of oblique detonation waves has been studied [25,26]; the higher temperature in the boundary layer of the induction region leads to an earlier onset of the overall ODW structure. Moreover, the presence of the boundary layer strengthens the oblique shock wave and boosts the formation of ODW [27]. Especially, compared with inviscid simulation, the triple-point moves upstream for abrupt transition ODW because of the shock/boundary-layer interaction [28]. The effects of turbulence intensities on the initiation and transition patterns were determined [29], and high turbulence intensity switches the abrupt transition to a smooth transition and shortens the initiation length, but insignificantly. Two separation bubbles possibly join together during the evolution of wedge-induced ODW, and the united separation zone expands further along the wedge surface, which causes ODW to propagate downstream and eventually flow out of the wedge [30]. Considering a realistic combustor, the separation zone induced by the ODW/boundary-layer interaction plays a vital role in the types of combustion mode in the combustor, and a stabilized overdriven normal detonation wave is simultaneously observed in the combustor [31,32]. Thus, the viscous effect cannot be neglected for the ODW evolution, and certain viscous hydrodynamic structures should be resolved in the numerical study.

Although certain approaches, such as hot jets [23,24] and multi-wedges [21], are presented to boost the initiation of ODW, the verifications are conducted with inviscid simulations. To shorten the induction length of the ODW, a cavity-based wedge, which is two finite-length wedges equipped with a cavity, is proposed here, and viscous detonation simulations are performed to determine the flowfield for the current geometric configuration. The high-resolution numerical method is adopted to solve the Reynolds-averaged Navier–Stokes (RANS) equation coupled with Spalart–Allmaras turbulence model and the two-step chemical reaction. An inflow Mach number ranging from 4.0 to 6.0 is selected to study the initiation and evolution characteristics of ODWs with the cavity-based wedge. Two high-temperature regions, the recirculation zone in the cavity and postshock due to shock/shock interaction, can promote the ignition; detonation initiation is also triggered via shock focus under certain inflow Mach numbers. The development of separation bubbles downstream and in the cavity should be considered for the anchor of ODW.

II. Numerical Method and Computation Setup

A. Governing Equations and Discretization

In this study, two-dimensional reactive Navier–Stokes equations coupled with a two-step chemical chain-branching kinetics model are employed, and the nondimensional formation in curvilinear coordinates is [33]

$$\frac{\bar{\boldsymbol{W}}}{\partial t}+\frac{\bar{\boldsymbol{F}}}{\partial \xi}+\frac{\bar{\boldsymbol{G}}}{\partial \eta}=\frac{1}{Re_\infty}\left(\frac{\bar{\boldsymbol{F}}_v}{\partial \xi}+\frac{\bar{\boldsymbol{G}}_v}{\partial \eta}\right)+\bar{\boldsymbol{S}} \tag{1}$$

with

$$\begin{gathered}\bar{\boldsymbol{W}}=J^{-1}\boldsymbol{W},\ \ \bar{\boldsymbol{F}}=J^{-1}(\xi_x\boldsymbol{F}+\xi_y\boldsymbol{G}),\ \ \bar{\boldsymbol{G}}=J^{-1}(\eta_x\boldsymbol{F}+\eta_y\boldsymbol{G}),\\ \bar{\boldsymbol{F}}_v=J^{-1}(\xi_x\boldsymbol{F}_v+\xi_y\boldsymbol{G}_v),\ \ \bar{\boldsymbol{G}}_v=J^{-1}(\eta_x\boldsymbol{F}_v+\eta_y\boldsymbol{G}_v),\ \ \bar{\boldsymbol{S}}=J^{-1}\boldsymbol{S}\end{gathered} \tag{2}$$

where $\boldsymbol{W}$ is the conservative solution vector, $\boldsymbol{F}$ and $\boldsymbol{G}$ are the convective terms, $\boldsymbol{F}_v$ and $\boldsymbol{G}_v$ are the diffusive terms, and $\boldsymbol{S}$ is the reaction source term. Where

$$\begin{aligned}\boldsymbol{W}&=[\rho\quad \rho u\quad \rho v\quad \rho E\quad \rho\lambda_I\quad \rho\lambda_R]^T,\\ \boldsymbol{F}&=[\rho u\quad \rho u^2+p\quad \rho uv\quad (\rho E+p)u\quad \rho u\lambda_I\quad \rho u\lambda_R]^T,\\ \boldsymbol{G}&=[\rho v\quad \rho uv\quad \rho v^2+p\quad (\rho E+p)v\quad \rho v\lambda_I\quad \rho v\lambda_R]^T,\\ \boldsymbol{F}_v&=\left[0\quad \tau_{xx}\quad \tau_{xy}\quad u\tau_{xx}+v\tau_{xy}+k_{\text{eff}}\frac{\partial T}{\partial x}\quad \rho D_{\text{eff}}\frac{\partial \lambda_I}{\partial x}\quad \rho D_{\text{eff}}\frac{\partial \lambda_R}{\partial x}\right]^T,\\ \boldsymbol{G}_v&=\left[0\quad \tau_{yx}\quad \tau_{yy}\quad u\tau_{yx}+v\tau_{yy}+k_{\text{eff}}\frac{\partial T}{\partial y}\quad \rho D_{\text{eff}}\frac{\partial \lambda_I}{\partial y}\quad \rho D_{\text{eff}}\frac{\partial \lambda_R}{\partial y}\right]^T,\\ \boldsymbol{S}&=[0\quad 0\quad 0\quad 0\quad \rho\omega_I\quad \rho\omega_R]^T\end{aligned} \tag{3}$$

and a coordinate transformation from (x, y) to (ξ, η) is processed with the following grid metric,

$$J^{-1} = \left|\frac{\partial(x,y)}{\partial(\xi,\eta)}\right|, \quad \xi_x = J\cdot y_\eta, \quad \xi_y = -J\cdot x_\eta,$$
$$\eta_x = -J\cdot y_\xi, \quad \eta_y = J\cdot x_\xi \tag{4}$$

The variables used in the preceding equations have their usual meanings: ρ, u, v, E, and p are the density, x-direction velocity, y-direction velocity, total energy per mass, and pressure, respectively. The equation of state can be expressed as

$$p = (\gamma-1)\rho\left[E - \frac{u^2+v^2}{2} + \lambda_R Q\right] \tag{5}$$

where Q is the energy released in the chemical reaction.

Following our previous work [34], the two-step chemical reaction model is used here, and λ_I and λ_R denote progress variables for the induction zone and exothermic reaction zone with values between 0 and 1. The chemical reaction ratios are ω_I and ω_R, which are defined as follows [35]:

$$\omega_I = -K_I H(\lambda_I)\exp\left(-\frac{E_a}{RT}\right),$$
$$\omega_R = K_R[1-H(\lambda_I)](1-\lambda_R)^\upsilon,$$
$$H(\lambda_I) = \begin{cases} 1, & 0 < \lambda_I \le 1 \\ 0, & \lambda_I \le 0 \end{cases} \tag{6}$$

where E_a is the activation energy; υ is the reaction order, which is typically 0.5; $H(\lambda_I)$ is the Heaviside function, which turns off the progress of λ_I at the end of the induction zone; and K_I and K_R are pre-exponential factors used to control the induced reaction and heat-releasing reaction, respectively.

The shear stresses (τ_{xx}, τ_{xy}, and τ_{yy}) are expressed as follows:

$$\tau_{xx} = \frac{2}{3}\mu_{\text{eff}}\left(2\frac{\partial u}{\partial x} - \frac{\partial v}{\partial y}\right), \quad \tau_{yy} = \frac{2}{3}\mu_{\text{eff}}\left(2\frac{\partial v}{\partial y} - \frac{\partial u}{\partial x}\right),$$
$$\tau_{xy} = \tau_{yx} = \mu_{\text{eff}}\left(\frac{\partial u}{\partial y} + \frac{\partial v}{\partial x}\right) \tag{7}$$

where μ_{eff}, k_{eff}, and D_{eff} are the effective viscosity, thermal conductivity, and diffusion coefficients:

$$\mu_{\text{eff}} = \mu_l + \mu_t,$$
$$k_{\text{eff}} = k_l + k_t, k = \frac{\mu c_p}{Pr},$$
$$D_{\text{eff}} = D_l + D_t, D = \frac{\mu}{\rho Sc} \tag{8}$$

and the subscripts l and t indicate laminar and turbulence parameters; Pr and Sc are Prandtl number and Schmidt number, which are 0.72, 0.9, and 0.5, 0.5 for laminar and turbulence flows, respectively; the laminar viscosity μ_l can be obtained using Sutherland law, and the turbulence viscosity μ_t is determined using the turbulence model:

$$\mu_t = \rho\tilde{\nu} f_{v1}, \quad f_{v1} = \frac{\chi^3}{\chi^3 + c_{v1}^3}, \quad \chi = \frac{\tilde{\nu}}{\nu}, \quad \nu = \frac{\mu_l}{\rho} \tag{9}$$

where $\tilde{\nu}$ is the work variable of the Spalart–Allmaras model, which can be calculated via the following equation in the conservative form without a trip term [36]:

$$\frac{\partial\rho\tilde{\nu}}{\partial t} + \nabla\cdot(\rho\tilde{\nu}U) = \rho c_{b1}(1-f_{t2})\hat{S}\tilde{\nu} - \frac{1}{Re_\infty}\rho\left(c_{w1}f_w - \frac{c_{b1}}{\kappa^2}f_{t2}\right)\left(\frac{\tilde{\nu}}{d}\right)^2$$
$$+\frac{1}{Re_\infty\sigma}\left[\nabla\cdot((\mu_l+\rho\tilde{\nu})\nabla\tilde{\nu}) + c_{b2}\rho(\nabla\tilde{\nu})^2 - (\nu+\tilde{\nu})\nabla\rho\nabla\tilde{\nu}\right] \tag{10}$$

The related coefficients in the turbulence model can be found in Refs. [36,37].

All physical parameters in the governing equations are normalized by referring to the uniform freestream:

$$x = \frac{x^*}{l_{\text{ref}}}, \ y = \frac{y^*}{l_{\text{ref}}}, \ t = \frac{t^*}{l_{\text{ref}}/u_\infty}\rho = \frac{\rho^*}{\rho_\infty}, \ u = \frac{u^*}{u_\infty},$$
$$v = \frac{v^*}{u_\infty}, \ p = \frac{p^*}{p_\infty}, \ T = \frac{T^*}{T_\infty}, \ e = \frac{e^*}{u_\infty^2}, \ Q = \frac{Q^*}{u_\infty^2}, \ \Psi = \frac{\Psi^*}{R_\infty},$$
$$Ea = \frac{E_a^*}{u_\infty^2}, \ K_I = \frac{K_I^*}{u_\infty/l_{\text{ref}}}, \ \mu = \frac{\mu^*}{\mu_\infty}, \ k = \frac{k^*}{\mu_\infty R_\infty}, \ D = \frac{D^*}{\mu_\infty/\rho_\infty} \tag{11}$$

where the symbol $*$ denotes dimensional quantities, and the subscript ∞ indicates quantities under a free inflow stream. Reference velocity $u_\infty = \sqrt{p_\infty/\rho_\infty}$; reference temperature $T_\infty = p_\infty/(R_\infty\rho_\infty)$; Ψ is a gas constant or specific heat, given here as representative, and $K_R = K_I K_R^*/K_I^*$.

The convective fluxes are calculated by the fifth-order weighted essentially nonoscillatory (WENO) finite difference method [38] combined with a Riemann problem solver, the Roe-HLLE method [39,40]. To decrease numerical dissipation and improve the resolution efficiency of the origin WENO-JS scheme, the WENO-Z method is adopted here with the new smoothness indicators [41]. The discretization of viscous terms is processed by the fourth-order accuracy finite central differencing scheme in the least stencil not wider than the total width of the fifth-order WENO stencils with various Taylor expansion coefficients [42,43].

When the governing equations have been processed via spatial discretization, an ordinary equation is gained, which is solved by semi-implicit additive Runge–Kutta (ARK) methods. ARK methods can treat the stiffness issue caused by chemical reactions well, and the open-source package ARKode, which was developed by Lawrence Livermore National Laboratory [44], was embedded into our solver to fulfill the temporal discretization. The butcher table in the current ARK method is ARK4(3)6L[2]SA [45], which can achieve fourth-order accuracy in time marching. In particular, the message-passing interface standard for message passing (as implemented in the MPICH library [46]) is used in the numerical simulations to accelerate the computation speed.

B. Physical Model and Flow Condition

A schematic depiction of the computational domain is presented in Fig. 2. The angle of the leading wedge (labeled C0C1 in Fig. 2) with a length $L_{W1} = 7.0$ mm is fixed at $\theta_W = 25$ deg, and an aft wedge (labeled C4C5 in Fig. 2) $L_{W2} = 25.0$ mm in length is connected with a cavity (labeled C1C2C3C4 in Fig. 2), which has a ratio of length and depth $L/D = 4.0$ and a depth $D = 4.0$ mm. The trailing edge of the cavity has an anticlockwise turning $\theta_C = 26.57$ deg under the direction of the leading wedge. The ghost cell method is used to treat the physical boundary. The freestream is parallel to the horizontal direction, the west boundary is a supersonic inflow, and the north and east boundaries are zeroth-order extrapolation outflows. The surfaces of the wedge and cavity are no-slip adiabatic wall boundary conditions.

Based on the classic physicochemical values of hydrogen-air mixtures [35], the parameters of supersonic reactive flow are listed in Table 1. Different specific heat ratios have been considered to mimic the change in mixtures from the unburned state to the post-shock state and finally to the combustion product state. Specific heat c_p, c_v and specific gas constant of the mixtures, labeled Ψ, are functions of the progress variables

$$\Psi(\lambda_I,\lambda_R) = \Psi_u\lambda_I + \Psi_u(1-\lambda_I-\lambda_R) + \Psi_b\lambda_R \tag{12}$$

C. Code Validation and Grid Independence

Systematic numerical cases to examine the discontinuity, detonation unsteadiness, and turbulence flow are performed via the in-house

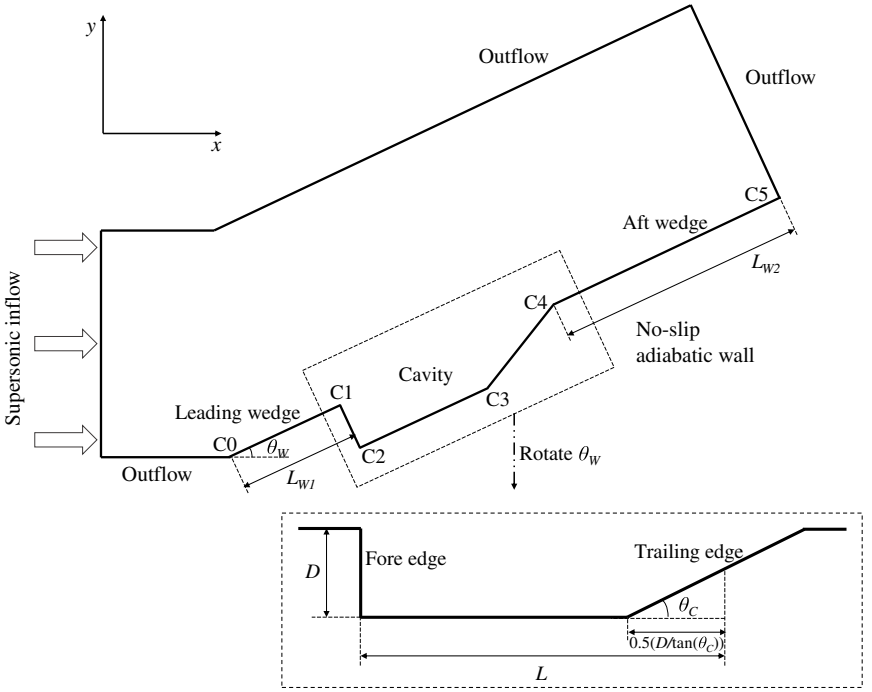

Fig. 2 Configuration and scale size of the computation domain.

solver, which achieves comparable results with theoretical or experimental values. The current high-resolution numerical method was also employed to determine the shock/combustion interaction of wedge-induced ODW in our previous study [34]. Representatively, the results of RANS simulation on cavity flow with $Ma = 3.0$ and two closeout angles [47] are given here, and the pressure profiles along the cavity wall are plotted in Fig. 3. The numerical results are consistent with the experimental values.

Grid-independence works have been conducted using a finite-length wedge-induced ODW, not a cavity-based wedge, with inflow Mach number 7.0, wedge angle 29.0 deg, and physicochemical parameters in Table 1. Nonuniform grids are used to perform numerical computation; the near-wall grid is refined (0.2 μm for the first-layer grid), and the aspect ratio of far-wall grid is unity with three grid sizes: 12.5, 20.0, 25.0 μm (labeled coarse, medium, and fine grids here). The temperature contours of the three-level grid are depicted in Figs. 4a–4c. It is found that the key features of the flow configurations can be captured with all grid sizes used. Due to the interaction between the incident shock wave emanating from the ODW triple point and the boundary layer on the wedge surface, a separation bubble is formed, which is captured for all grid sizes like other key features of the flowfields. The pressure and temperature profiles along the wedge surface are depicted in Fig. 4d, which assemble well, and the results of three grid sizes exhibit comparable tendencies. In addition, the dimensionless number y+ is introduced to characterize the near-wall mesh resolution, and y+ is nearly unity for $Ma = 7.0$ here. To balance the computation accuracy and cost, the grid size, which is 20.0 μm for the far-wall grid and 0.2 μm for the first-layer grid of the wall, is adopted in the following numerical studies.

Table 1 Physical-chemical parameters of mixtures

P_∞, Pa	1.0×10^5
T_∞, K	300
$\gamma_u, \gamma_s, \gamma_b$	1.40, 1.32, 1.16
R_u^*, R_s^*, R_b^*, J/(kg · K)	397.57, 397.00, 347.67
l_{ref}, m	3.5×10^{-4}
$Q^*/R_u^*T_\infty$	50.0
$E_a^*/R_u^*T_\infty$	50.0

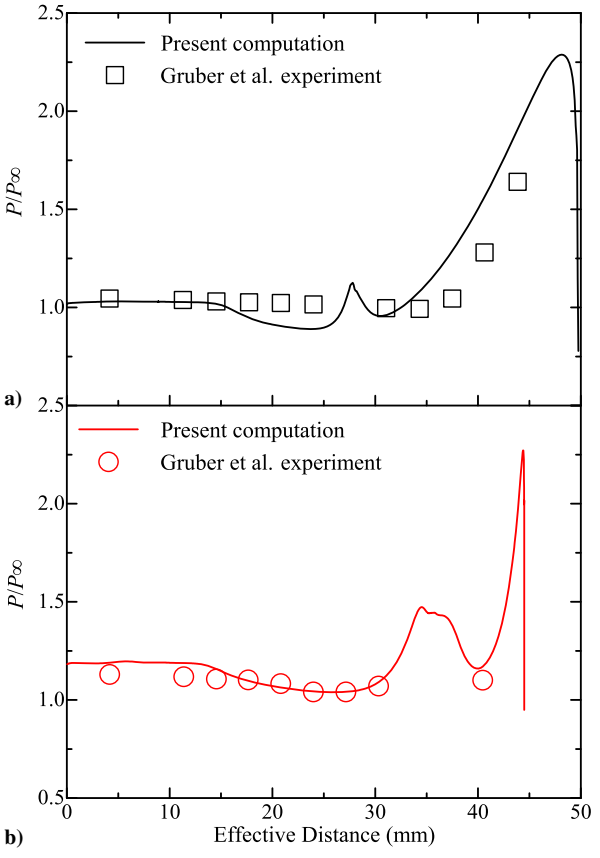

Fig. 3 Pressure profiles along the wall with inflow Mach number 3.0 and two closeout angles: a) 30.0 deg and b) 90.0 deg for a cavity with depth of 8.9 mm and length-to-depth ratio of 3.

III. Results and Discussion

A. Typical Flowfield Without Chemical Reaction

The flow configuration of the wedge mounted in a cavity without chemical reaction is analogous for varied inflow Mach numbers ranging from 4.0 to 6.0 here. The temperature contour and closed-up

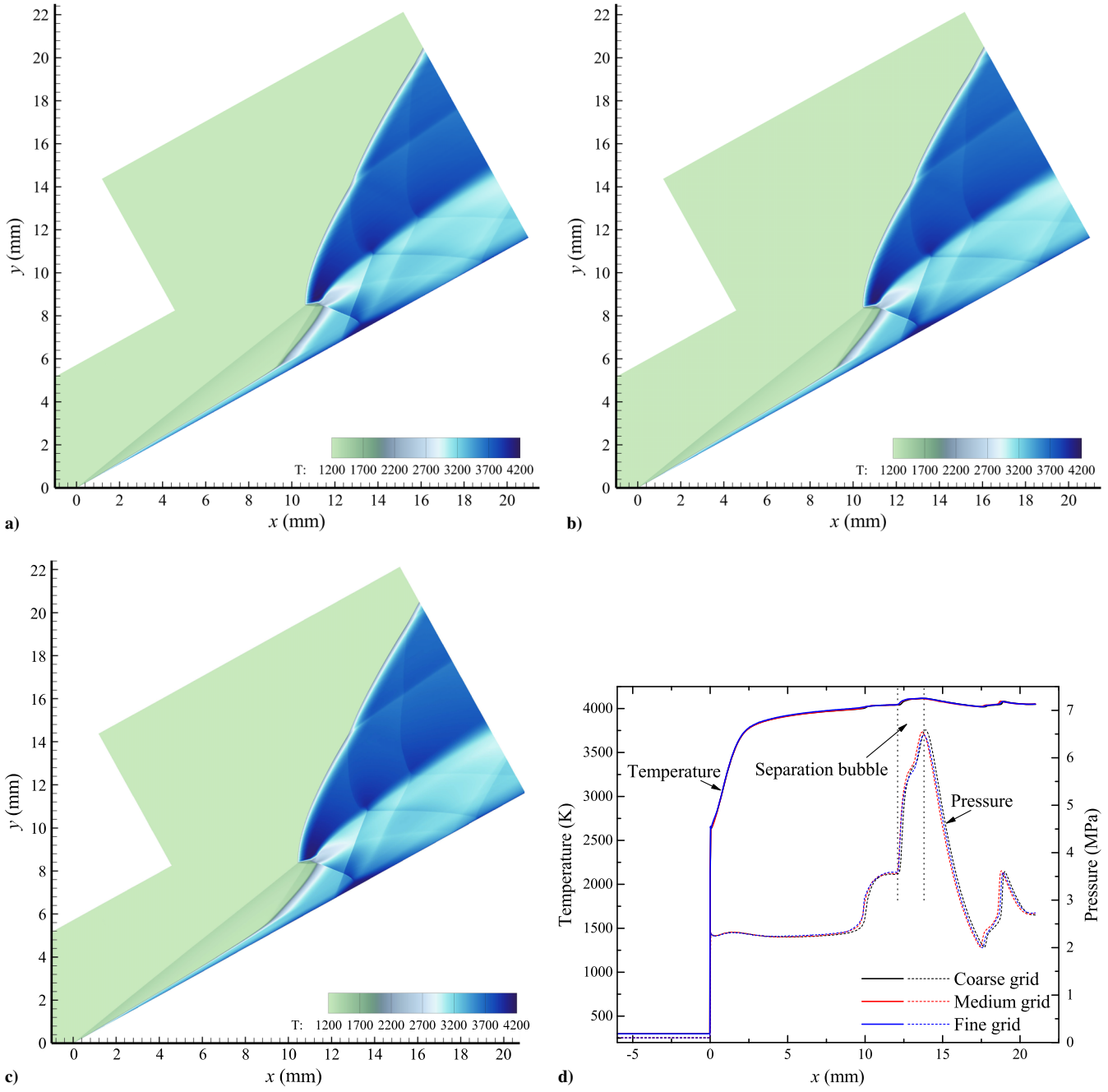

Fig. 4 Temperature contours, pressure, and temperature profiles along the wedge surface with inflow Mach number 7.0 and wedge angle 29.0 deg for three grid sizes: a) coarse, b) medium, and c) fine mesh grids.

schlieren image with $Ma = 4.0$ are shown in Fig. 5. Because there is a leading wedge before the cavity, a shock wave (SW), labeled OSW1 in Fig. 5, emanates from the wedge tip, and the Mach number of fluid flowing through the cavity is not 4.0 but about 2.18 because of the compression of OSW1. The principal flow feature near the cavity is similar to that reported by Heller and Delfs [48], in which a shear layer isolates the subsonic recirculation zone in the cavity from the supersonic coming flow. The numerical results capture certain typical wave phenomena, such as the expansion wave (EW) from the fore edge of the cavity, an unsteady shock wave/expansion wave from the shear layer, a rear OSW from the aft edge, and expansion fans (EF) from the outspread shoulder of the cavity. The SW and EW alternate when the shear layer experiences periodical "up-and-down" motion. Two vortices (the large primary vortex at the aft cavity and small secondary vortex at the fore cavity) in the recirculation zone can be visible from the numerical schlieren.

The obvious discrepancy of the flowfield between a sole cavity and a cavity-based wedge is the interaction of OSW1 emanating from the wedge tip with downstream waves driven by the cavity. The curved shock named OSW2 interacts with the rear OSW; Type I interaction occurs near the triple point, based on the classification of shock/shock interaction presented by Edney [49]; and a stronger shock, named TrOSW, is formed. It is well-known that chemical reactions are temperature-sensitive processes, and the high-temperature region behind strong shock waves promotes ignition. The flow variables along the streamline near the triple point with various Mach numbers ranging from 4.0 to 6.0 can be determined, to predict the induction ignition length $l_{\text{ign}} = u_{\text{OSW}} \cdot t_{\text{ind}}$ for simplicity. The calculated l_{ign} is given in Fig. 6, and the ignition length of simulation for $Ma = 7.0$ without a cavity is also plotted with a value of 84 mm, which is smaller than the theoretical value due to the effectiveness of the burning boundary layer. High Mach numbers tend to cause a higher postshock temperature, so the ignition length of a sole wedge for

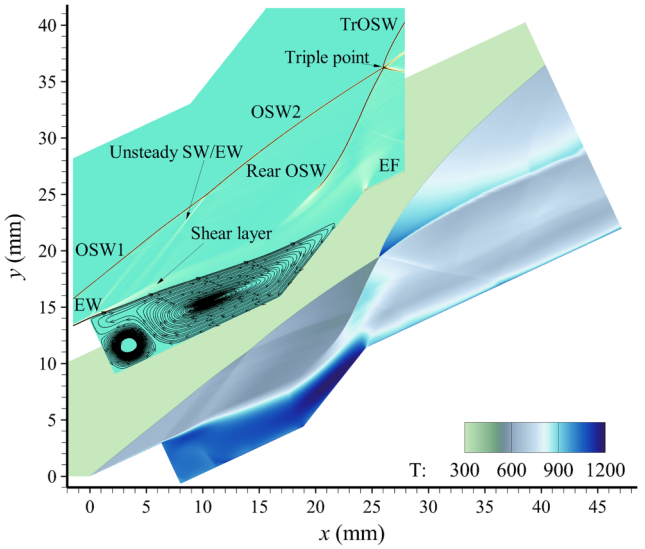

Fig. 5 Typical flow configuration (temperature contour and zoomed-in numerical schlieren) of a wedge embedded cavity under the condition of unreactive inflow, $Ma = 4.0$.

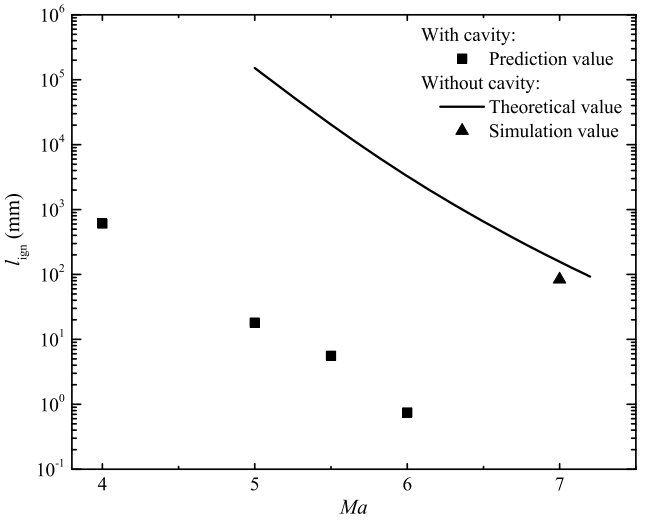

Fig. 6 Prediction value of the ignition lengths for various Mach numbers with and without cavity, $\theta_W = 25$ deg.

$Ma = 4.0 \sim 6.0$ is larger than 84 mm. However, the present simulation shows that the ignition length of the cavity-based wedge suffers a drastic reduction in l_{ign} compared with that of the wedge without a cavity. In particular, the high-temperature and low-velocity scenario in the recirculation zone of the internal cavity also contribute to the ignition. In the following sections, the evolution of combustion and detonation initiation are considered with various inflow Mach numbers.

B. Combustion Process with Various Mach Numbers

1. Mach 4.0 Inflow

Based on the unreactive flow, the wave configuration with the chemical reaction for $Ma = 4.0$ is numerically solved, as shown in Fig. 7. The predicted induction length behind TrOSW is ~609 mm, as reported in Fig. 6, which exceeds the computation domain here. Therefore, the recirculation zone bounded in the cavity can provide an ignition condition, and the elapsed dimensionless time is approximately 68.06 when the first ignition point appears. The accelerating flame surface spreads and grows outward, which creates a shock wave before the flame that collides with TrOSW and boosts the combustion behind TrOSW, but no detonation initiation is observed for $Ma = 4.0$. Eventually, the flame is maintained in the cavity and

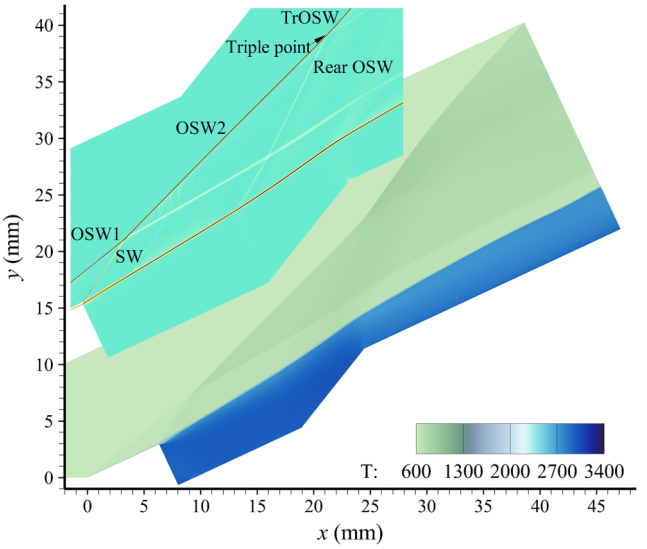

Fig. 7 Quasi-steady-state numerical results of a wedge embedded cavity with chemical reaction for $Ma = 4.0$.

expands to the near-wall region of the aft wedge. In the magnified numerical schlieren, the shock wave is noted at the fore edge of the cavity due to the dilatation of the high-temperature burned products in the cavity, where fluids should deflect upward. Sequentially, deflected flows behind SW or OSW2 need a weak rear OSW driven by the trailing edge to match downstream flows, and the shock intensity of rear OSW (defined by $(P_2 - P_1)/P_1$, where P_1, P_2 are the preshock and postshock pressure, respectively) decreases from 2.6 ($P_2 = 1.72$ MPa) to 0.26 ($P_2 = 0.97$ MPa) compared with that of unreactive flow configuration in Fig. 5. The interaction between OSW2 and weak rear OSW cause a weak TrOSW here.

Thus, there are two factors for the evolution of the reactive flow configuration: 1) shock collision, which occurs between the outward shock driven by the combustion in the cavity and shock wave OSW2 or TrOSW; the shock collision can rapidly increase the temperature and enhance the ignition; and 2) the weak shock (TrOSW); the rear OSW is weakened when the flame stretches outward from the cavity and interacts with OSW2 near the triple point, which results in a weak TrOSW, which cannot sufficiently compress and heat the unburned reactants to trigger the release of chemical energy. Two competing factors affect the ignition and detonation initiation of supersonic, reactive flow, and more numerical simulations with higher Mach numbers will be performed to examine which factor plays the dominant role.

2. Mach 5.0 Inflow

The temperature contours and close-up numerical shadowgraphs at selected times for $Ma = 5.0$ are given in Fig. 8. Ignition first occurs in the cavity, and the heat-released region is mainly attached at the trailing edge of the cavity. Then, the flame will spread outward and move to the front cavity (see Fig. 8a); the compressible wave before the flame surface can be clearly visible from the numerical schlieren, which is strengthened via the postfront energy supplied by chemical reaction. The compressible wave must collide with OSW2 and TrOSW, and the ignition point emerges after the collision (labeled SF1), as shown in Fig. 8b. Simultaneously, the flame surface eventually strikes the fore edge of the cavity and reflects between the fore and bottom edges, which contributes to the bulge of the regional shear layer and introduces more disturbances. Behind the previous TrOSW, two reactive waves (RWs) are developed into different formations (decoupled and coupled) at this instant (as depicted in Fig. 8c), and another collision between two RWs inevitably occurs. Consequently, detonation initiation at SF2 is acquired, as shown in Fig. 8d. Three collisions described in Figs. 8c and 8d are captured here. The profiles of the shock front for the additional shock focuses (SF3~SF5) are visible in the magnified view of Fig. 8d. The collision

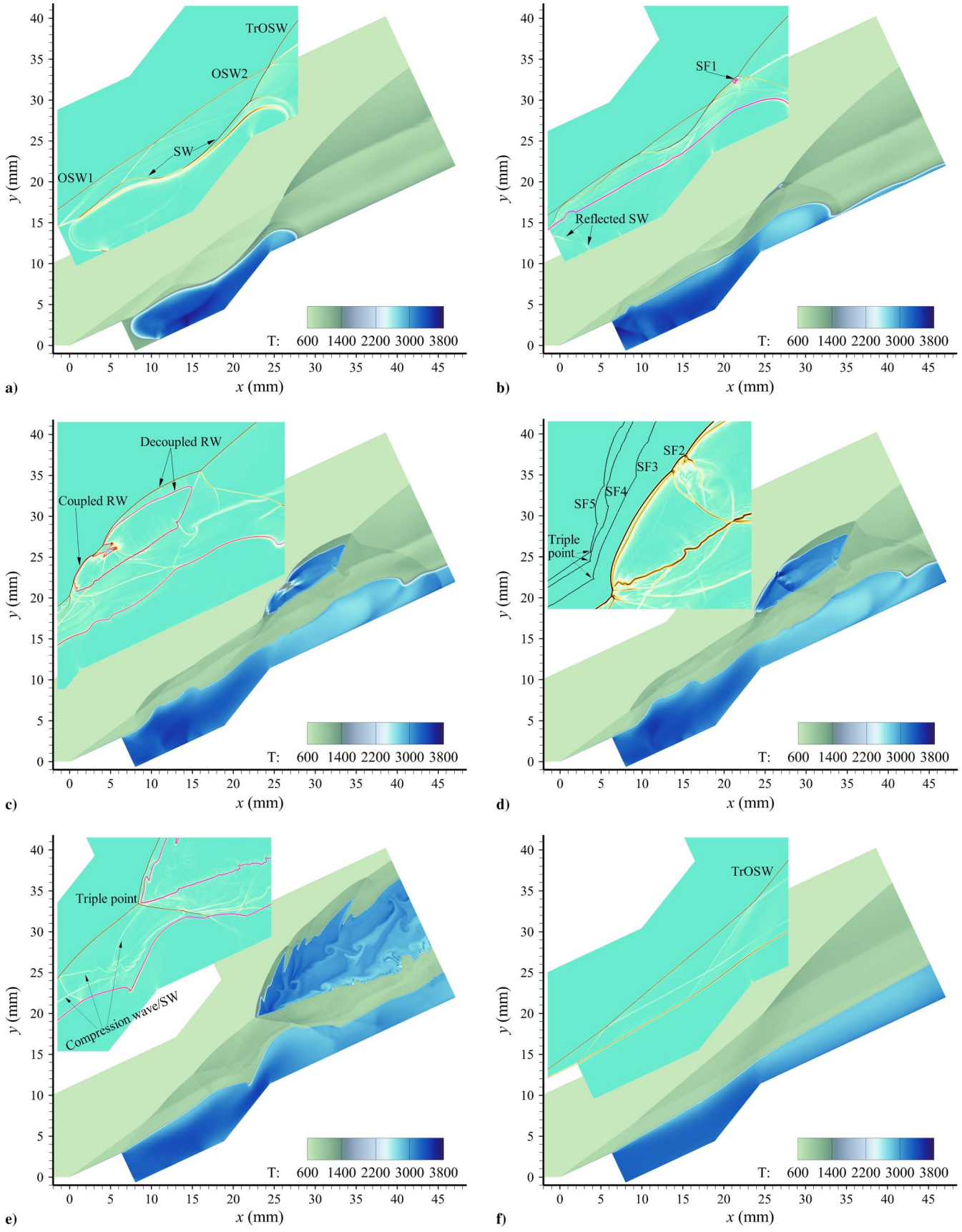

Fig. 8 Evolution of the onset of detonation with $Ma = 5.0$ at different nondimensional time snapshots of a) 3.553, b) 6.321, c) 10.779, d) 11.640, e) 22.840, and f) 167.322 (purple solid line: product mass fraction, $\lambda_R = 0.05$).

locations gradually move to the triple point, and an oblique detonation wave is transitorily set up only near the triple point. The leading shock and chemical reaction are decoupled along the shock front (see Fig. 8e). It is supposed that the leading shock wave cannot sufficiently compress to maintain preheating effects and support the detonation combustion, but the pressure disturbances that originate

from the cavity flame interact with the decoupled reactive wave and temporarily trigger new detonation near the triple point, which cannot imperishably anchor. When the compressible waves/shock waves produced by the cavity-driven combustion flow out, the flame behind TrOSW is blown out, as shown in Fig. 8f, and the flame only exists in the recirculation zone of the cavity and following wall (aft wedge), which is similar to that of $Ma = 4.0$.

To illustrate the change in state of unburned reactants when two shocks collide, an analysis is performed with the assumed control volume, where the region scale is $50 \times 50\ \mu m^2$. The profiles of temperature and deposition energy rate versus nondimensional time during five shock collisions are depicted in Fig. 9. The monitoring time includes several periods such as unburned reactants, shock collisions, detonation initiation, and passing through of products. Figure 9a shows the change trends of temperature. The unburned combustible is compressed by shock waves at location P1, and the chemical energy is swiftly released at location P2, where the temperatures gain a sharp increase. The specific chemical energy and total energy, which are defined as effective chemical energy released per kg of reactant $\lambda_R Q$ and the sum of internal energy, kinetic energy, and chemical energy $(p/(\gamma-1)\rho) + (u^2 + v^2/2) - \lambda_R Q$, respectively, and the rate of two kinds of given deposition energy can be noted in Fig. 9b. The maximum specific total energy rate approximately locates in the location P1 in Fig. 9a, where the internal energy and kinetic energy dramatically increase due to the shock focus; the value is up to the shock strength, ‘ the second shock collision SF2 is more severe than the others. Sequentially, the peak chemical energy rate suffers a short delay, which corresponds to location P2 in Fig. 9a and amounts of chemical heat released when detonation takes place. Based on the evolution of ODW in Fig. 8, SF1 is a typical shock-shock focus, triggering the combustion, and SF2 is essentially a collision of two reactive waves, initiating the detonation. Specifically, for SF1 and 2, a delay exists between the starting points of peak total energy rate and peak chemical energy rate. SF3–5 can be treated as a preparatory period of the transverse wave evolution along the detonation front for the weakly sustainable ODW; the turbulence intensity behind ODW front is thereby augmented. Because of that, the turbulent diffusion can promote the ignition of unburned mixtures, especially for the irregular detonation [50]. This is a possible reason why the starting points of two peaks for SF3–5 are close compared to SF1 and 2.

According to the quantitative analysis of the energy rate with a control volume, the shock focus can motivate 10^6 J magnitude energy release in a tiny area and timescale, which directly triggers the detonation initiation. It is supposed that the shock collision deposits sufficient energy in the preheated reactants to evoke an expeditious ignition, which acts in a similar manner to the direct detonation initiation [51]. As discussed in Fig. 8, shock collision first occurs when the shock created by the accelerating flame in the cavity interacts with the downstream shocks (such as TrOSW), and rapid combustion follows the first shock focus (SF1). In addition, more shock collisions are observed between two reactive waves (see SF2 to SF5 in Fig. 8d). Although detonation initiation is acquired by shock collision, a sustainable ODW cannot be established, inasmuch as the leading shock of detonation wave cannot preserve powerful compression strength to preheat the particles that pass through the shock front and induce a chemical reaction. To stabilize an ODW, the intensity of TrOSW should be sufficiently strong; otherwise, the leading shock front and chemical reaction zone of the detonation wave would be decoupled, and combustion would be sustained only in the cavity and the following aft wedge.

3. *Mach 6.0 Inflow*

With an enlarged Mach number ($Ma = 6.0$), a quasi-steady flow configuration of standing ODW can be obtained, and numerical results at various snapshots are depicted in Fig. 10. As predicted in the previous sections, a shorter l_{ign} is required for $Ma = 6.0$, and swift ignitions occur from the internal cavity and post-TrOSW. Obviously, the detonation is established without the aid of shock collision under the current condition, but the effects of the shock focus on the evolution of flow configuration should be considered, and the triple point will more rapidly proceed upstream. A Mach stem, which appears near the triple point of ODW, interferes with the flame front along the shear layer of the cavity and forms a tiny separation bubble, where the sonic lines, reattachment shock wave, and streamlines are visible in Fig. 10a. Consequently, the separation

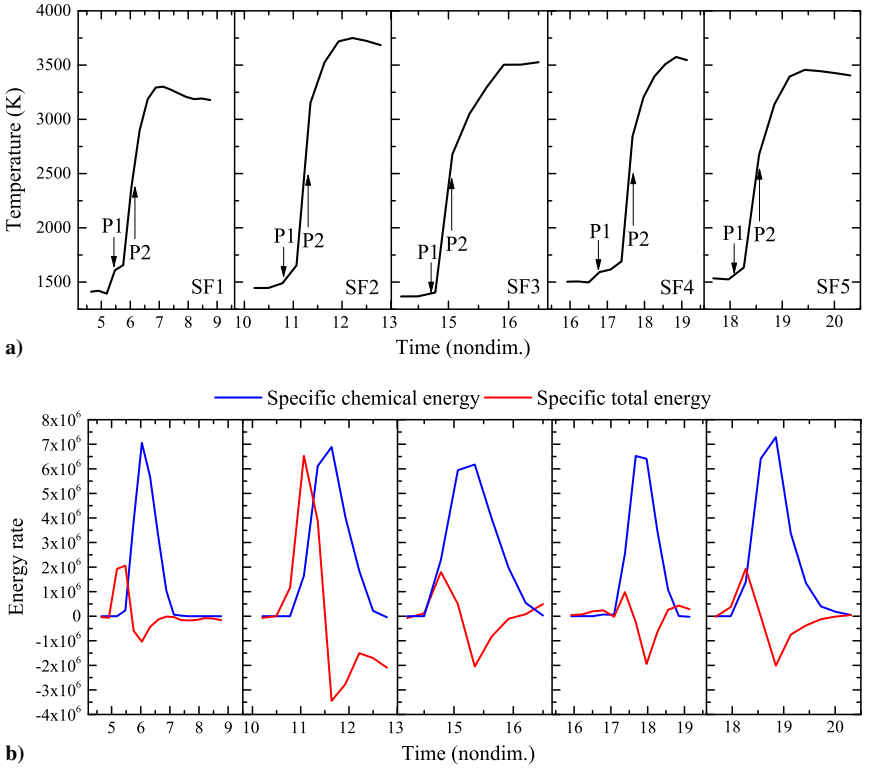

Fig. 9 Changes in a) temperature and b) energy rate during the shock focus period with $Ma = 5.0$.

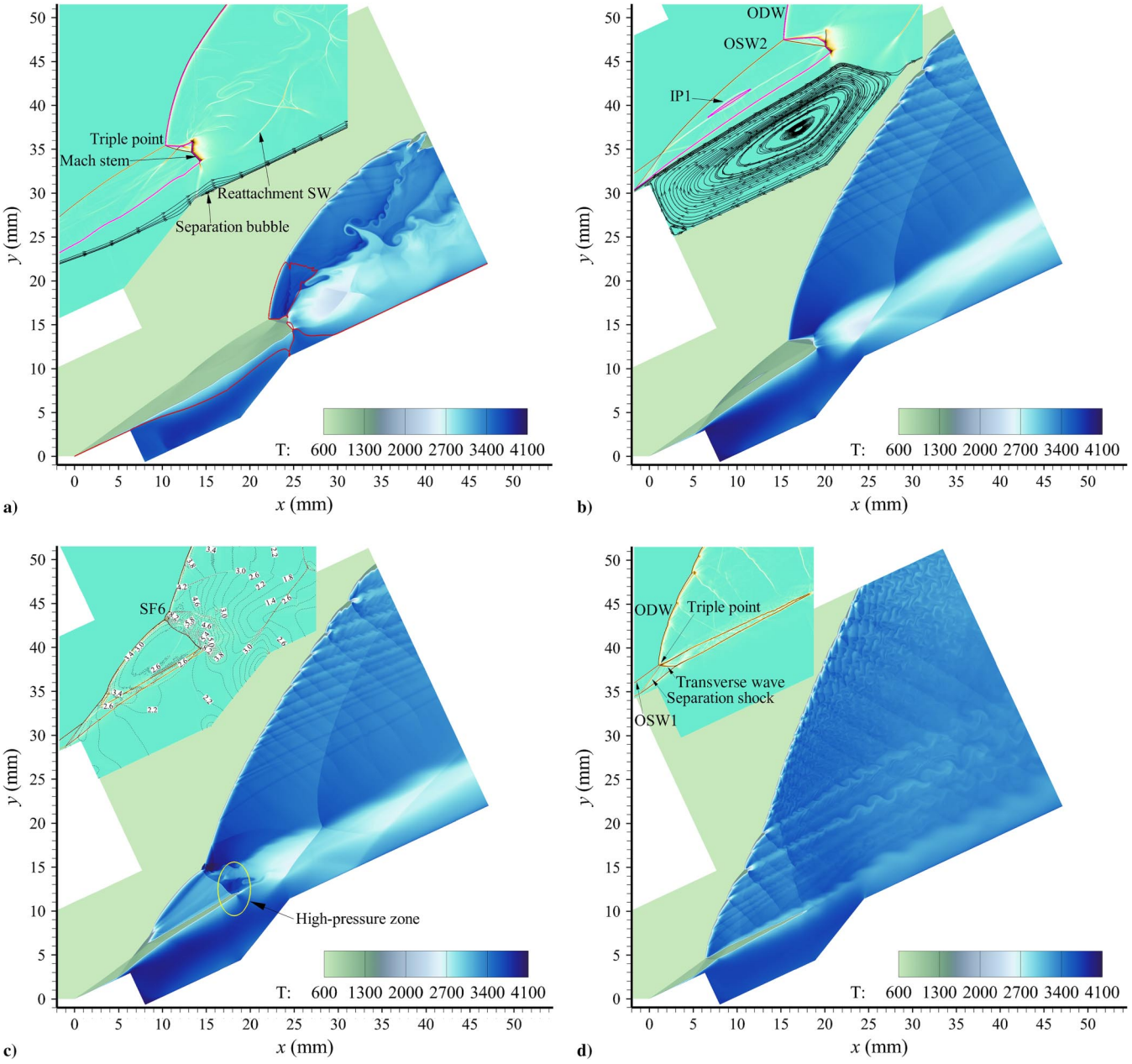

Fig. 10 Evolution of the onset of detonation with $Ma = 6.0$ at different nondimensional time snapshots of a) 10.883, b) 46.780, c) 51.585, and d) 193.589 (solid line: purple, product mass fraction, $\lambda_R = 0.05$; red, sonic line $Ma = 1.0$).

bubble flows into the cavity, due to the continuous upstream movement of the triple point, and merges with the primary vortex of the internal cavity. As shown in Fig. 10b, the primary vortex in the cavity significantly grows, and a small separation zone appears on the leading wedge near the fore edge of the cavity, which contributes to a stronger OSW2. Then, the chemical induction process behind OSW2 is accelerated, and an ignition point (IP) IP1 emerges. The flame front expands outward from IP1 and collides with the ODW and Mach stem downstream, which results in a direct detonation initiation SF6, as depicted in Fig. 10c. The overlaid isoline of pressure of 0.6–11.0 MPa with an interval 0.4 MPa is given in the magnified numerical shadowgraph. Particularly, it can be concluded that the area above the shear layer of the cavity possesses high pressure because of heat release and shock/reactive wave collision; the development of the primary vortex in the cavity is efficiently suppressed, and the primary vortex shrinks and eventually almost binds to the cavity. A quasi-steady flowfield, where a new triple point uniting OSW1, separation shock, and ODW is formed near the fore cavity, can be discerned in the numerical shadowgraph (see Fig. 10d). It is supposed that the standing ODW is set up even if the triple point would experience oscillation due to the interaction of the transverse wave and shear layer.

Furthermore, Fig. 11 shows the length of the flame surface during the full ignition process with varied inflow Mach numbers. An enlarged Mach number can shorten the delay time and boost the development of shock-induced combustion behind TrOSW. The flame surfaces for $Ma = 4.0$ and 5.0 have similar final length because the cavity-driven combustion is dominant here. Attributed to the high temperature of the cavity and post-TrOSW for $Ma = 6.0$, the flame rapidly develops as soon as the numerical computation starts. In particular, the combustion fronts driven by cavity and TrOSW-induced combustion combine in a short time, so a sharp decrease following the jump of flame surface length can be found at the early period. Another peak appears in Fig. 11 due to the new ignition point behind OSW2. The cellular-like structure on the ODW front and upward–backward movement of the triple point make the flame surface exhibit certain fluctuations compared with those of $Ma = 4.0$ and 5.0 during the late stage of combustion evolution.

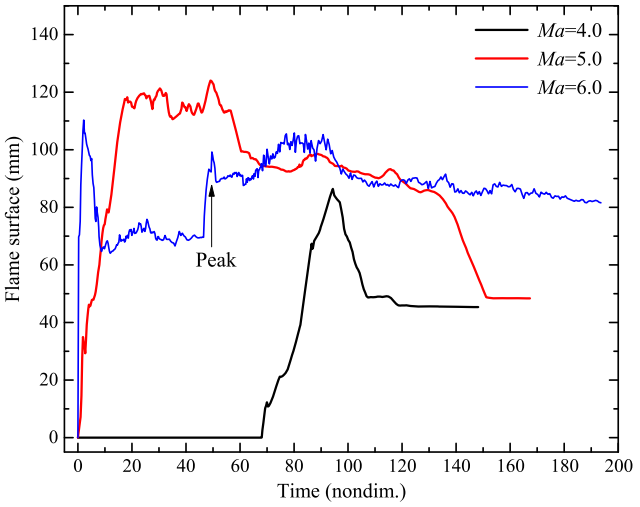

Fig. 11 Flame surface length at different dimensionless times with Mach numbers of 4.0, 5.0, and 6.0.

C. Effects of Separation Bubble

Additional numerical simulation with $Ma = 5.5$ is conducted to illustrate that the development of the separation zone plays a momentous role in the standing of ODW, as shown in Fig. 12. The primary ignition procedure behind TrOSW and in the cavity is similar to that of $Ma = 5.0$ and 6.0. With the moderate compression performance of Mach 5.5 inflow, TrOSW-induced detonation and cavity-driven combustion occur, but there is no chemical reaction between slip lines (SLs) SL1 and SL2 (also the combustion interface, see Fig. 12a), which exhibits a notable discrepancy compared with that of $Ma = 6.0$. The flow configuration can only be momentarily maintained, and the transverse wave emanating from the ODW front interacts with SL1, SL2, and the wall to induce combustion (see ignition point IP2 in Fig. 12a). The combustion between SL1 and SL2 results in the formation of another strong SW behind the reattachment SW, which contributes to the similar phenomena of thermal choke, as depicted in Fig. 12b. Similarly, the grown primary vortex in the cavity spills out and strengthens OSW2, which leads to an ignition behind OSW2 as described in the case $Ma = 6.0$. Nevertheless, the high-pressure zone is not present above the cavity here, which cannot limit the

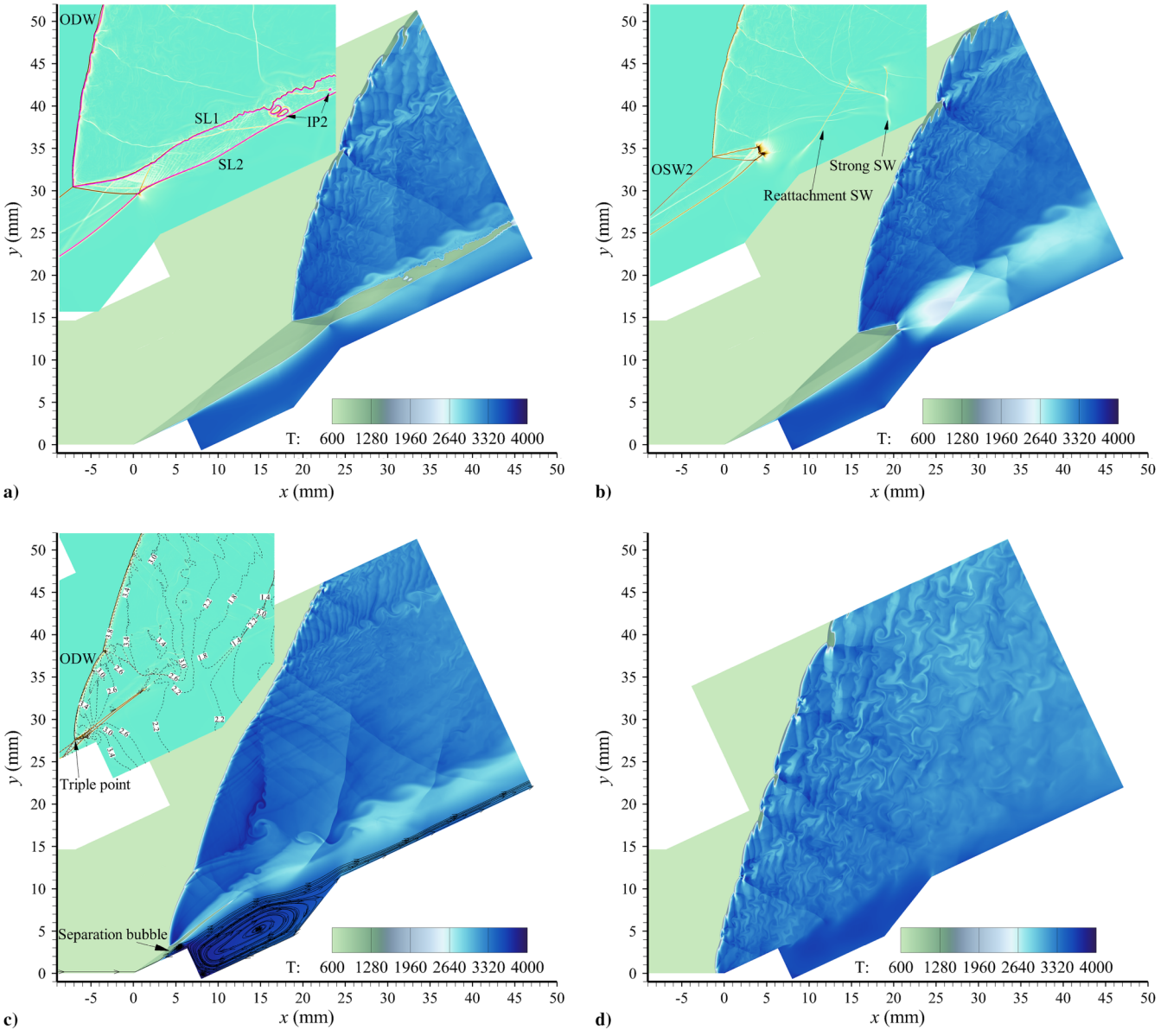

Fig. 12 Detached process of oblique detonation waves with $Ma = 5.5$ at different nondimensional time snapshots of a) 132.866, b) 158.724, c) 182.124, and d) 264.722 (purple solid line: product mass fraction, $\lambda_R = 0.05$).

primary vortex in the cavity. Consequently, the ODW front marches upstream, and a separation bubble is formed and developed on the leading wedge (see Fig. 12c). Under the joint effects of separation bubble on the leading wedge and recirculation zone in the cavity, the ODW front is pushed upstream along the leading wedge and eventually detached from the wall in a quasi-steady-state manner, as given in Fig. 12d.

The skin-friction coefficient C_f with $Ma = 5.5$ at the selected time is depicted in Fig. 13a. The distance between the locations of the zero-friction coefficient may be defined as the maximum length of the separation bubble (SB). Three separation zones can be determined on the leading and aft wedges: one (labeled SB1) is located on the leading wedge due to the dilatation of the recirculation zone of the cavity, and the others are near the shoulder of the cavity (labeled SB2) and on the aft wedge downstream (labeled SB3) because of shock/boundary-layer interactions. The location and length of the separation bubble L_{SB} versus nondimensional time are organized in bubble charts for $Ma = 5.5$ and 6.0, where the circle scale is characterized by L_{SB}, as shown in Figs. 13b and 13c. For both inflow Mach numbers, SB2 diminishes and moves to the cavity shoulder since this separation bubble flows into the cavity. The evolution of the separation bubble at this stage is similar, but the subsequent development of the separation zone and wave configuration depends on the scenarios of pressure downstream for two inflow Mach numbers.

As shown in Fig. 14, the tendencies of wall pressure during the period to merge two separation zones and expand the recirculation zone in the cavity are shown in subfigures Figs. 14a-i/14b-i and Figs. 14a-ii/14b-ii, respectively. Focusing on the process by which the separation bubble near the shoulder flows into the cavity, the summit wall pressure of the cavity obviously increases. For $Ma = 5.5$, a new ignition point occurring between slip lines SL1 and SL2 will lead to an incident shock wave on the aft wedge, where a new separation bubble SB3 can be noted in Fig. 13b, and a distinct apex pressure appears at location P_{peak} in Fig. 14a-i, which acts as a high back pressure for the cavity here. Then, the similar choke phenomena occur, and more mass is added into the cavity, which contributes to the violent development of the recirculation zone in the cavity. The averaged pressure of the cavity wall suffers an increase from 1.57 to 2.25 MPa for $Ma = 5.5$; that is, there is an obvious jump compared with that for $Ma = 6.0$ (from 1.73 to 2.12 MPa) during the period in Figs. 14a-i/14b-i. Sequentially, the recirculation zone in the cavity will expand outward in various manners. For $Ma = 6.0$, the pressure of the aft wedge remains at a low level (see the right section of C4 in Fig. 14b-ii), and the mass in the cavity mostly flows out downstream due to the high-pressure zone above the cavity in Fig. 10c. Simultaneously, a separation shock near the fore edge of the cavity is formed and moves upstream with a short distance on the leading wedge, and a small separation bubble SB1 can be determined from Fig. 13c. In contrast, for $Ma = 5.5$, the pressure downstream has decreased but remains at a high level (see $t = 165.541 \sim 176.580$ in Fig. 14a-ii), and the strong shock-induced separation bubble SB3 exists during this period. The recirculation zone in the cavity is dilated to the region of the leading wedge, and separation bubble SB1 is formed and expands on the leading wedge (see SB1 in Fig. 13b), which pushes the separation shock upstream until the detonation wave is detached. The peak pressure along the trailing edge of the cavity contiguously reduces when the vortex in the cavity expands, as plotted in Figs. 14a-ii/14b-ii.

Additionally, the detached angle for the inflow condition ($Ma = 5.5$, $Q = 50.0$, $\gamma_1 = 1.4$, and $\gamma_2 = 1.16$) is nearly 21.14 deg, which is smaller than the leading wedge angle. It is another explanation of

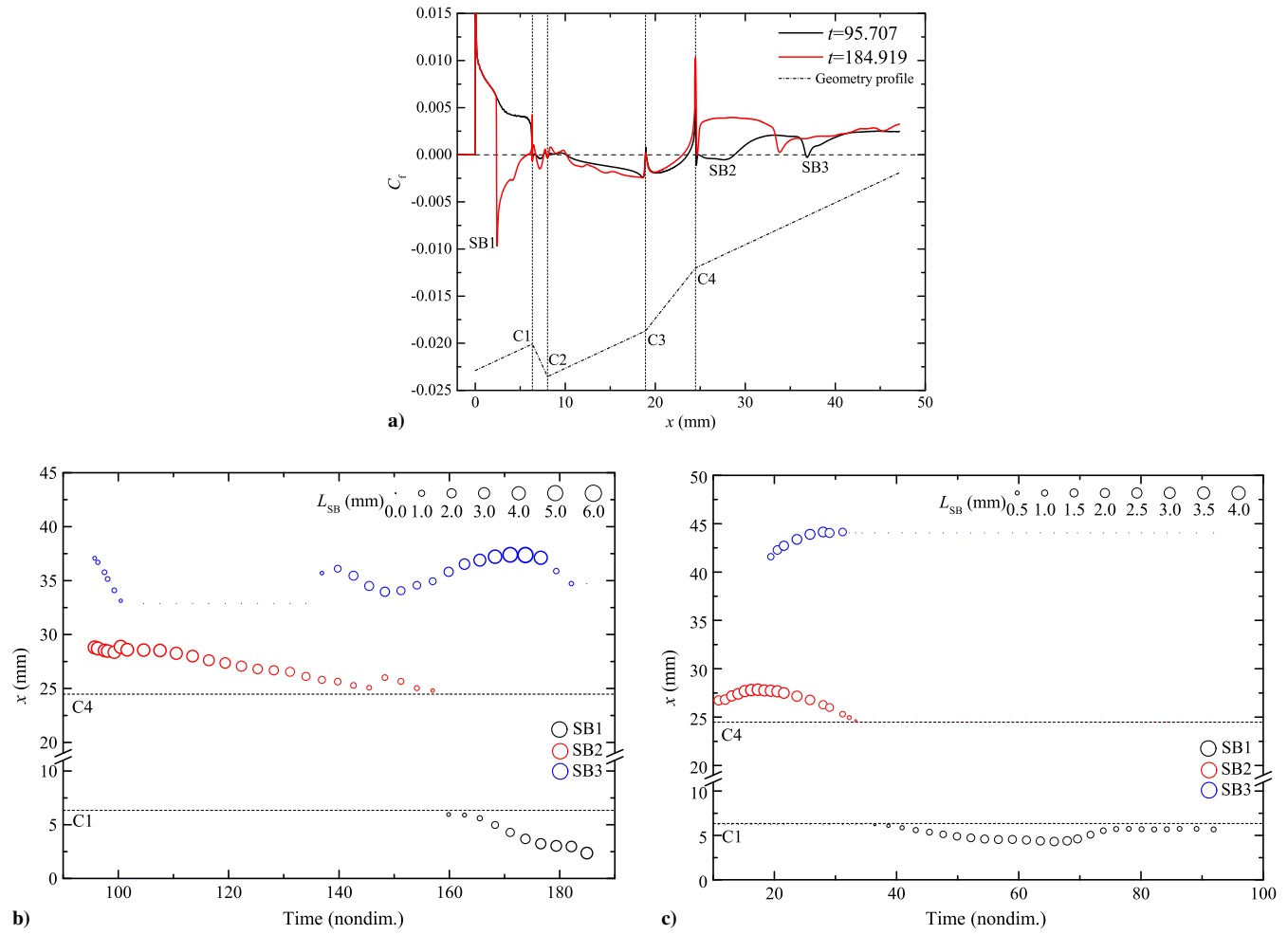

Fig. 13 a) Typical skin-friction coefficient along the solid wall for $Ma = 5.5$; change tendency of three separation bubbles for b) $Ma = 5.5$ and c) $Ma = 6.0$ (C1C2, C2C3, and C3C4 are the fore, bottom, and trailing edges of the cavity, respectively).

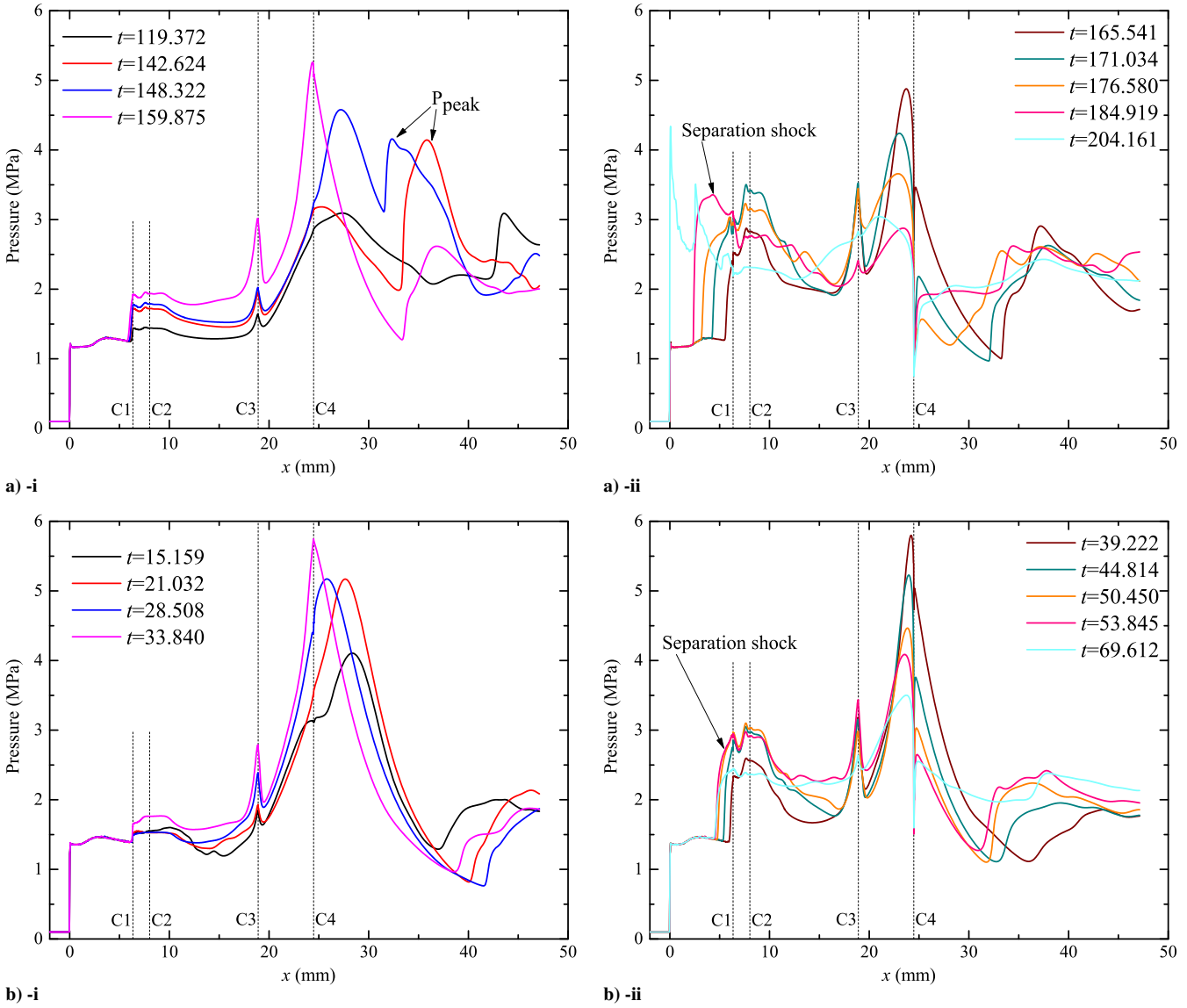

Fig. 14 Pressure profiles of the wall boundary at selected time snapshots with Mach numbers a) 5.5 and b) 6.0 (C1C2, C2C3, and C3C4 are the fore, bottom, and trailing edges of the cavity, respectively).

the detached ODW at the point of the detonation polar line. A small amount of heat release can be selected when the inflow Mach number decreases to enlarge the detached angle of the ODW polar line. Certain flow-control technologies, such as suction slots, can be adopted to suppress the development of separation bubbles. With this proposal, the standing ODW may be established, and a further numerical study is required to verify this supposition in the future.

IV. Conclusions

A high-resolution numerical method that adopts WENO-Z reconstruction and the additive Runge–Kutta method is employed to solve the Reynolds-averaged Navier–Stokes equation with the Spalart–Allmaras turbulence model and a two-step chemical reaction. Investigations on the shock-induced combustion of a cavity-based wedge with inflow Mach numbers ranging from 4.0 to 6.0 are performed, and the mechanism of detonation initiation for the cavity-based wedge is preliminarily illustrated. The representative unreactive flow for a wedge embedded cavity with $Ma = 4.0$ is similar to that of the single cavity reported in the literature except for the shock/shock interaction downstream, where a triple point unites the oblique shock wave (OSW) that emanates from the leading wedge tip, the rear OSW created by the trailing edge of the cavity, and a strong shock wave named TrOSW. Considering the chemical reaction, the evolution of the ignition and flow configuration exhibits different tendencies when the Mach numbers increase from 4.0 to 6.0, and combustion preliminarily emerges in two regions: 1) cavity-driven combustion and 2) shock-induced combustion behind TrOSW. The shock intensity of TrOSW and the development of the separation zone can affect the initiation and standing characteristics of cavity-based wedge-induced ODW.

When $Ma = 4.0$ and 5.0, the final flow configurations are similar, where flames are bounded in the cavity and along the near-wall area of the aft wedge. Additionally, multiple detonation initiations with the aid of shock collision are observed for $Ma = 5.0$. The first shock focus is triggered by the shock wave that originates from the cavity-driven accelerating flame and TrOSW downstream, and the others take place on the front of TrOSW-induced combustion, where reactive waves propagate along the front and collide with each other. In particular, the expanded flame in the cavity can weaken the rear OSW from the trailing edge of the cavity, and the shock intensity of TrOSW diminishes. For $Ma = 6.0$, a nearly direct initiation behind TrOSW is achieved without shock collision. Owing to the upstream march of the ODW triple point, the separation bubble downstream, which is caused by the interaction between the incident shock-aligned ODW triple point and wedge surface, flows into the cavity. The dilative recirculation zone in the cavity strengthens the separation shock and leads to new ignition, and a triple point of ODW is renewed above the

fore edge of the cavity. Another computation with $Ma = 5.5$ is conducted: delayed ignition occurs at the unburned region between the near-wall flame of the aft wedge and TrOSW-induced combustion, which results in phenomena similar to thermal choking, and the ODW front is pushed upstream and eventually detached.

According to numerical studies, the proposed geometric configuration, a cavity-based wedge, can sharply decrease the ignition length compared with that of a sole wedge and contribute to the formation of an ODW, which is a potential consideration of the ODWE design for a wide-range Mach number. However, further work should be done based on the current preliminary study. More numerical computations and theoretical analysis are required to determine an optimum geometric configuration of the cavity-based wedge that can establish an ODW under low Mach numbers. A controllable location of standing ODW is also a challenge for the engineering application of ODWEs.

Acknowledgments

The research is supported by the National Natural Science Foundation of China under grant numbers U2141220 and 11672309.

References

[1] Lee, J. H. S., *The Detonation Phenomenon*, Cambridge Univ. Press, Cambridge, England, U.K., 2008.

[2] Wolański, P., "Detonative Propulsion," *Proceedings of the Combustion Institute*, Vol. 34, No. 1, 2013, pp. 125–158. https://doi.org/10.1016/j.proci.2012.10.005

[3] Kailasanath, K., "Review of Propulsion Applications of Detonation Waves," *AIAA Journal*, Vol. 38, No. 9, 2000, pp. 1698–1708. https://doi.org/10.2514/2.1156

[4] Urzay, J., "Supersonic Combustion in Air-Breathing Propulsion Systems for Hypersonic Flight," *Annual Review of Fluid Mechanics*, Vol. 50, No. 1, 2018, pp. 593–627. https://doi.org/10.1146/annurev-fluid-122316

[5] Dudebout, R., Sislian, J. P., and Oppitz, R., "Numerical Simulation of Hypersonic Shock-Induced Combustion Ramjets," *Journal of Propulsion and Power*, Vol. 14, No. 6, 1998, pp. 869–879. https://doi.org/10.2514/2.5368

[6] Chan, J., Sislian, J. P., and Alexander, D., "Numerically Simulated Comparative Performance of a Scramjet and Shcramjet at Mach 11," *Journal of Propulsion and Power*, Vol. 26, No. 5, 2010, pp. 1125–1134. https://doi.org/10.2514/1.48144

[7] Jiang, Z., Zhang, Z., Liu, Y., Wang, C., and Luo, C., "Criteria for Hypersonic Airbreathing Propulsion and Its Experimental Verification," *Chinese Journal of Aeronautics*, Vol. 34, No. 3, 2021, pp. 94–104. https://doi.org/10.1016/j.cja.2020.11.001

[8] Viguier, C., da Silva, L. F. F., Desbordes, D., Deshaies, B., da Silva, L. F. F., Desbordes, D., and Deshaies, B., "Onset of Oblique Detonation Waves: Comparison Between Experimental and Numerical Results for Hydrogen-Air Mixtures," *Symposium (International) on Combustion*, Vol. 26, No. 2, 1996, pp. 3023–3031. https://doi.org/10.1016/S0082-0784(96)80146-9

[9] Kasahara, J., Fujiwara, T., Endo, T., and Arai, T., "Chapman-Jouguet Oblique Detonation Structure Around Hypersonic Projectiles," *AIAA Journal*, Vol. 39, No. 8, 2001, pp. 1553–1561. https://doi.org/10.2514/2.1480

[10] Teng, H., Ng, H. D., and Jiang, Z., "Initiation Characteristics of Wedge-Induced Oblique Detonation Waves in a Stoichiometric Hydrogen-Air Mixture," *Proceedings of the Combustion Institute*, Vol. 36, No. 2, 2017, pp. 2735–2742. https://doi.org/10.1016/j.proci.2016.09.025

[11] Yang, P., Teng, H., Jiang, Z., and Ng, H. D., "Effects of Inflow Mach Number on Oblique Detonation Initiation with a Two-Step Induction-Reaction Kinetic Model," *Combustion and Flame*, Vol. 193, July 2018, pp. 246–256. https://doi.org/10.1016/j.combustflame.2018.03.026

[12] Figueria Da Silva, L. F., and Deshaies, B., "Stabilization of an Oblique Detonation Wave by a Wedge: A Parametric Numerical Study," *Combustion and Flame*, Vol. 121, Nos. 1–2, 2000, pp. 152–166. https://doi.org/10.1016/S0010-2180(99)00141-8

[13] Miao, S., Zhou, J., Liu, S., and Cai, X., "Formation Mechanisms and Characteristics of Transition Patterns in Oblique Detonations," *Acta Astronautica*, Vol. 142, Jan. 2018, pp. 121–129. https://doi.org/10.1016/j.actaastro.2017.10.035

[14] Teng, H., Zhang, Y., and Jiang, Z., "Numerical Investigation on the Induction Zone Structure of the Oblique Detonation Waves," *Computers and Fluids*, Vol. 95, May 2014, pp. 127–131. https://doi.org/10.1016/j.compfluid.2014.03.001

[15] Liu, Y. S., Liu, Y. S., Wu, D., and Wang, J. P., "Structure of an Oblique Detonation Wave Induced by a Wedge," *Shock Waves*, Vol. 26, No. 2, 2016, pp. 161–168. https://doi.org/10.1007/s00193-015-0600-5

[16] Verreault, J., Higgins, A. J., and Stowe, R. A., "Formation of Transverse Waves in Oblique Detonations," *Proceedings of the Combustion Institute*, Vol. 34, No. 2, 2013, pp. 1913–1920. https://doi.org/10.1016/j.proci.2012.07.040

[17] Teng, H., Ng, H. D., Li, K., Luo, C., and Jiang, Z., "Evolution of Cellular Structures on Oblique Detonation Surfaces," *Combustion and Flame*, Vol. 162, No. 2, 2015, pp. 470–477. https://doi.org/10.1016/j.combustflame.2014.07.021

[18] Yang, P., Teng, H., Ng, H. D., and Jiang, Z., "A Numerical Study on the Instability of Oblique Detonation Waves with a Two-Step Induction-Reaction Kinetic Model," *Proceedings of the Combustion Institute*, Vol. 37, No. 3, 2019, pp. 3537–3544. https://doi.org/10.1016/j.proci.2018.05.090

[19] Bhattrai, S., and Tang, H., "Formation of Near-Chapman-Jouguet Oblique Detonation Wave over a Dual-Angle Ramp," *Aerospace Science and Technology*, Vol. 63, April 2017, pp. 1–8. https://doi.org/10.1016/j.ast.2016.12.010

[20] Papalexandris, M. V., "A Numerical Study of Wedge-Induced Detonations," *Combustion and Flame*, Vol. 120, No. 4, 2000, pp. 526–538. https://doi.org/10.1016/S0010-2180(99)00113-3

[21] Qin, Q., and Zhang, X., "A Novel Method for Trigger Location Control of the Oblique Detonation Wave by a Modified Wedge," *Combustion and Flame*, Vol. 197, Nov. 2018, pp. 65–77. https://doi.org/10.1016/j.combustflame.2018.07.011

[22] Qin, Q., and Zhang, X., "Study on the Effects of Geometry on the Initiation Characteristics of the Oblique Detonation Wave for Hydrogen-Air Mixture," *International Journal of Hydrogen Energy*, Vol. 44, No. 31, 2019, pp. 17004–17014. https://doi.org/10.1016/j.ijhydene.2019.04.248

[23] Li, H., Li, J., Xiong, C., Fan, W., Zhao, L., and Han, W., "Investigation of Hot Jet on Active Control of Oblique Detonation Waves," *Chinese Journal of Aeronautics*, Vol. 33, No. 3, 2020, pp. 861–869. https://doi.org/10.1016/j.cja.2019.09.026

[24] Qin, Q., and Zhang, X., "Study on the Initiation Characteristics of the Oblique Detonation Wave by a Co-Flow Hot Jet," *Acta Astronautica*, Vol. 177, June 2020, pp. 86–95. https://doi.org/10.1016/j.actaastro.2020.07.015

[25] Li, C., Kailasanath, K., and Oran, E., "Effects of Boundary Layers on Oblique-Detonation Structures," *31st Aerospace Sciences Meeting*, AIAA Paper 1993-0450, 1993. https://doi.org/10.2514/6.1993-450

[26] Choi, J.-Y., and Jeung, I.-S., "Numerical Simulation of Super-Detonative Ram Accelerator: Its Shock-Induced Combustion and Oblique Detonation," *Hypervelocity Launchers. Shock Wave Science and Technology Reference Library*, Vol. 10, edited by F. Seiler, and O. Igra, Springer, Cham, Switzerland, 2016, pp. 217–267. https://doi.org/10.1007/978-3-319-26018-1

[27] Bachman, C. L., and Goodwin, G. B., "Ignition Criteria and the Effect of Boundary Layers on Wedge-Stabilized Oblique Detonation Waves," *Combustion and Flame*, Vol. 223, Jan. 2021, pp. 271–283. https://doi.org/10.1016/j.combustflame.2020.10.007

[28] Fang, Y., Zhang, Z., and Hu, Z., "Effects of Boundary Layer on Wedge-Induced Oblique Detonation Structures in Hydrogen-Air Mixtures," *International Journal of Hydrogen Energy*, Vol. 44, No. 41, 2019, pp. 23429–23435. https://doi.org/10.1016/j.ijhydene.2019.07.005

[29] Yu, M., and Miao, S., "Initiation Characteristics of Wedge-Induced Oblique Detonation Waves in Turbulence Flows," *Acta Astronautica*, Vol. 147, June 2018, pp. 195–204. https://doi.org/10.1016/j.actaastro.2018.04.022

[30] Miao, S., Xu, D., Song, T., and Yu, J., "Shock Wave-Boundary Layer Interactions in Wedge-Induced Oblique Detonations," *Combustion Science and Technology*, Vol. 192, No. 12, 2020, pp. 2345–2370. https://doi.org/10.1080/00102202.2019.1646256

[31] Zhang, Z., Ma, K., Zhang, W., Han, X., Liu, Y., and Jiang, Z., "Numerical Investigation of a Mach 9 Oblique Detonation Engine with Fuel Pre-Injection," *Aerospace Science and Technology*, Vol. 105, Oct. 2020, Paper 106054. https://doi.org/10.1016/j.ast.2020.106054

[32] Zhang, Z., Wen, C., Zhang, W., Liu, Y., and Jiang, Z., "Formation of Stabilized Oblique Detonation Waves in a Combustor," *Combustion and Flame*, Vol. 223, Jan. 2021, pp. 423–436. https://doi.org/10.1016/j.combustflame.2020.09.034

[33] Blazek, J., *Computational Fluid Dynamics: Principles and Applications*, 3rd ed., Butterworth-Heinemann, Oxford, 2015. https://doi.org/10.1016/B978-0-08-099995-1.00002-6

[34] Yang, L., Yue, L., Zhang, Q., and Zhang, X., "Numerical Study on the Shock/Combustion Interaction of Oblique Detonation Waves," *Aerospace Science and Technology*, Vol. 104, Sept. 2020, Paper 105938. https://doi.org/10.1016/j.ast.2020.105938

[35] Leung, C., Radulescu, M. I., and Sharpe, G. J., "Characteristics Analysis of the One-Dimensional Pulsating Dynamics of Chain-Branching Detonations," *Physics of Fluids*, Vol. 22, No. 12, 2010, Paper 126101. https://doi.org/10.1063/1.3520188

[36] Allmaras, S. R., and Johnson, F. T., "Modifications and Clarifications for the Implementation of the Spalart-Allmaras Turbulence Model," *Seventh International Conference on Computational Fluid Dynamics (ICCFD7)*, ICCFD7-1902, Big Island, Hawaii, 2012, pp. 1–11.

[37] Spalart, P., and Allmaras, S., "A One-Equation Turbulence Model for Aerodynamic Flows," *30th Aerospace Sciences Meeting and Exhibit*, AIAA Paper 1992-0439, 1992. https://doi.org/10.2514/6.1992-439

[38] Jiang, G. S., and Shu, C. W., "Efficient Implementation of Weighted ENO Schemes," *Journal of Computational Physics*, Vol. 126, No. 1, 1996, pp. 202–228. https://doi.org/10.1006/jcph.1996.0130

[39] Roe, P. L., "Approximate Riemann Solvers, Parameter Vectors, and Difference Schemes," *Journal of Computational Physics*, Vol. 135, No. 2, 1997, pp. 250–258. https://doi.org/10.1006/jcph.1997.5705

[40] Einfeld, B., "On Godunov-Type Methods for Gas Dynamics," *SIAM Journal on Numerical Analysis*, Vol. 25, No. 2, 1988, pp. 294–318. https://doi.org/10.1137/0725021

[41] Acker, F., Borges, R. R., and Costa, B., "An Improved WENO-Z Scheme," *Journal of Computational Physics*, Vol. 313, May 2016, pp. 726–753. https://doi.org/10.1016/j.jcp.2016.01.038

[42] Shen, Y., Wang, B., and Zha, G., "Implicit WENO Scheme and High Order Viscous Formulas for Compressible Flows," *25th AIAA Applied Aerodynamics Conference*, AIAA, Reston, VA, 2007, pp. 1756–1773. https://doi.org/10.2514/6.2007-4431

[43] Sun, Z.-S., Ren, Y.-X., Zhang, S.-Y., and Yang, Y.-C., "High-Resolution Finite Difference Schemes Using Curvilinear Coordinate Grids for DNS of Compressible Turbulent Flow over Wavy Walls," *Computers & Fluids*, Vol. 45, No. 1, 2011, pp. 84–91. https://doi.org/10.1016/j.compfluid.2010.12.022

[44] Hindmarsh, A. C., Brown, P. N., Grant, K. E., Lee, S. L., Serban, R., Shumaker, D. E., and Woodward, C. S., "SUNDIALS: Suite of Nonlinear and Differential/Algebraic Equation Solvers," *ACM Transactions on Mathematical Software*, Vol. 31, No. 3, 2005, pp. 363–396. https://doi.org/10.1145/1089014.1089020

[45] Kennedy, C. A., and Carpenter, M. H., "Additive Runge-Kutta Schemes for Convection-Diffusion-Reaction Equations," *Applied Numerical Mathematics*, Vol. 44, Nos. 1–2, 2003, pp. 139–181. https://doi.org/10.1016/S0168-9274(02)00138-1

[46] Gropp, W., Lusk, E., and Skjellum, A., *Using MPI: Portable Parallel Programming with the Message-Passing Interface*, MIT Press, Cambridge, MA, 1994.

[47] Gruber, M. R., Baurle, R. A., Mathur, T., and Hsu, K. Y., "Fundamental Studies of Cavity-Based Flameholder Concepts for Supersonic Combustors," *Journal of Propulsion and Power*, Vol. 17, No. 1, 2001, pp. 146–153. https://doi.org/10.2514/2.5720

[48] Heller, H., and Delfs, J., "Cavity Pressure Oscillations: The Generating Mechanism Visualized," *Journal of Sound and Vibration*, Vol. 196, No. 2, 1996, pp. 248–252. https://doi.org/10.1006/jsvi.1996.0480

[49] Edney, B., "Anomalous Heat Transfer and Pressure Distributions on Blunt Bodies at Hypersonic Speeds in the Presence of an Impinging Shock," Flygtekniska Forsoksanstalten (The Aeronautical Research Institute of Sweden) TR FFA-115, Stockholm, Sweden, 1968.

[50] Radulescu, M. I., "A Detonation Paradox: Why Inviscid Detonation Simulations Predict the Incorrect Trend for the Role of Instability in Gaseous Cellular Detonations?" *Combustion and Flame*, Vol. 195, Sept. 2018, pp. 151–162. https://doi.org/10.1016/j.combustflame.2018.05.002

[51] Goodwin, G. B., and Oran, E. S., "Premixed Flame Stability and Transition to Detonation in a Supersonic Combustor," *Combustion and Flame*, Vol. 197, Nov. 2018, pp. 145–160. https://doi.org/10.1016/j.combustflame.2018.07.008

C. Wen
Associate Editor